ARCHIVES OF ELECTRICAL ENGINEERING VOL. X(Y), pp. 1-22 (2026)

This paper has been accepted for publication in the AEE journal. This is the version, which has not been fully edited and content may change prior to final publication.
Citation information: DOI 10.24425/aee.2026.158257

Coordinated protection of RC-Crowbar and energy storage systems for enhanced low-voltage ride-through in wind turbines

TAIGUO LI*, WANYIN GONG, CAIXIA TAO

School of Automation and Electrical Engineering, Lanzhou Jiaotong University
No.88, Anning West Road, Lanzhou, People's Republic of China
e-mail: leetg@lzjtu.edu.cn

Abstract: With the widespread adoption of doubly-fed induction generators (DFIGs) in power grids, the enhancement of their low-voltage ride-through (LVRT) capability has become critically important for grid stability, especially under conditions of severe voltage sags. This study proposes a coordinated control strategy that integrates an improved RC-Crowbar circuit with a hybrid energy storage system (HESS) to enhance DFIG LVRT capability. Unlike conventional crowbars that absorb large reactive power during faults, the improved RC-Crowbar leverages capacitor-based reactive power support to reduce DFIG reactive power demand and accelerate fault current decay. Meanwhile, the HESS provides dynamic voltage support and reactive power compensation, which results in improved DC-link voltage stability and a more optimised power response from the stator and rotor. The performance of the proposed approach was evaluated under diverse grid fault conditions using a DFIG wind turbine model constructed in the MATLAB/Simulink environment to verify its effectiveness. From the simulation results as shown, it means that the RC-Crowbar can reduce the DC-link voltage fluctuations, restrain the rotor overcurrent, and also helps to speed up the recovery. And combined with the HESS, combined with the coordinated protection scheme can also improve and coordinate voltage stability and reduce power oscillation and other improvements, which will further improve the overall DFIG system LVRT performance.

Key words: coordinated protection, DFIG, HESS, LVRT, RC-Crowbar circuit

Nomenclature

P_{MPPT}	MPPT-based active power reference	V_{dc}^{ref}	Reference DC-link voltage
P_s	Stator active power	V_{dc}	Actual DC-link voltage
i_{rd}	*d*-axis component of rotor current	P_{dp}^{ref}	Active power dispatching command
i_{rd}^{ref}	Reference *d*-axis rotor current	P_{out}	Output active power of system

This paper has been accepted for publication in the AEE journal. This is the version, which has not been fully edited and content may change prior to final publication.
Citation information: DOI 10.24425/aee.2026.158257

V_{rd}	d-axis component of rotor voltage	i_{gd}^{ref}	Reference d-axis grid current
V_{rq}	q-axis component of rotor voltage	i_{gd}	d-axis component of grid current
Q_s^{ref}	Reference stator reactive power	$V_{gd-\text{comp}}$	d-axis compensated grid voltage
Q_s	Stator reactive power	V_{gd}	d-axis component of grid voltage
i_{rq}^{ref}	Reference q-axis rotor current	V_{pcc}	Point of common coupling voltage
i_{rq}	q-axis component of rotor current	P_{sc}	Supercapacitor output power
Q_{out}	System output reactive power	U_{sc}	Supercapacitor voltage
i_{gq}^{ref}	Reference q-axis grid current	I_{sc}	Supercapacitor current
i_{gq}	q-axis component of grid current	P_{tur}	Turbine generation power
V_{gq}	q-axis component of grid voltage	P_{bat}	Battery output power
I_{bat}	Battery current	ω_r	Rotor electrical angular speed
V_{pcc}^{ref}	Point of common coupling voltage reference	ω_s	Synchronous angular speed
$V_{gq-\text{comp}}^{\text{ref}}$	q-axis compensated grid voltage reference	C_{bat}	Battery capacity
$V_{gd-\text{comp}}^{\text{ref}}$	d-axis compensated grid voltage reference	U_s	Stator voltage magnitude
Q_{dp}^{ref}	Reactive power dispatching command		

1. Introduction

Global energy consumption continues to rise while conventional fossil fuel resources are dwindling. Consequently, advancing and harnessing renewable energy sources has emerged as a central pillar of international energy strategies [1]. Wind power stands out as a key renewable resource that helps tackle the dual challenges of carbon emission reduction and energy security. Key advantages, including low cost, high efficiency, and a straightforward structure, have positioned the DFIG as a predominant choice in the wind power generation sector. However, the

This paper has been accepted for publication in the AEE journal. This is the version, which has not been fully edited and content may change prior to final publication.
Citation information: DOI 10.24425/aee.2026.158257

centralized construction of wind farms and their large-scale grid integration pose severe challenges to the stability of the power grid. Grid stability and the safe operation of wind turbines are directly contingent upon their LVRT performance. This reliance becomes especially critical when the grid experiences significant voltage sags [2]. Therefore, current research aimed at enhancing the LVRT capability of DFIGs predominantly concentrates on two key areas: the optimisation of control algorithms and the integration of dedicated hardware protection circuitry [3–5].

Regarding improvements in control strategies, Luo *et al*. explored the interaction between the rotor-side converter (RSC) and grid-side converter (GSC) in DFIG systems, subsequently proposing an LVRT control strategy that relies on their coordinated current control [6]. To improve the LVRT performance, Marri *et al*. investigated the transient response of the phase-locked loop (PLL) in conjunction with the phase jump phenomena in the DFIG's terminal voltage following a fault, thereby optimising the control strategy [7]. Moreover, the introduction of a hybrid optimisation algorithm served to augment the adaptive neuro-fuzzy inference system (ANFIS)-based direct power control (DPC) strategy. This enhancement led to significant gains in the system's control performance while also establishing its LVRT capability [8, 9]. In their work, Guan *et al*. tackled the issue of asymmetrical LVRT in weak grids. They proposed a novel small-signal model for a dual-sequence PLL, modelled as an equivalent two-degree-of-freedom (2-DOF) spring-damper particle system, ultimately leading to improved dynamic stability [10]. Essentially, an enhanced control strategy aims to precisely manage the voltage-current relationship by optimising key parameter values. This optimisation allows the wind turbine system to independently handle the excess energy produced during grid fault events. Nevertheless, when a severe grid voltage dip occurs, the DFIG system has difficulty absorbing the excess energy. Therefore, employing an external protection circuit to absorb the surplus energy is a more effective measure [11, 12].

Regarding additional hardware protection circuits, Gu *et al*. propose a Triple Active Bridge (TAB)-based excitation converter with a series-parallel DC-link configuration, replacing the conventional capacitive DC-link to enhance LVRT capability under severe fault conditions [13]. Gu *et al*. proposed a multifunctional capacitive bridge-type fault current limiter (MCBFCL) that operates based on a variable capacitance principle. This feature enables it to both facilitate active power transfer in normal states and bolster LVRT performance during grid faults [14]. Liang *et al*. propose optimising the stator-side series impedance by adjusting the resistance value through reactive power regulation to enhance LVRT capability [15]. Furthermore, several studies have demonstrated that integrating superconducting fault current limiters (SFCLs), along with their various configurations, into the DC link of the RSC is an effective method for enhancing the LVRT performance of DFIGs [16–18]. The crowbar protection circuit, owing to its simple structure and ease of control, is widely adopted in DFIGs to achieve LVRT [19–21]. Some researchers enhance LVRT capability by modifying the crowbar circuit, specifically by changing its energy dissipation bypass from a purely resistive circuit to a resistor-capacitor (RC) circuit [22, 23]. Wang D. *et al*. proposed a comprehensive strategy to bolster the fault ride-through (FRT) performance of DFIGs under both symmetrical and asymmetrical fault conditions. This strategy

This paper has been accepted for publication in the AEE journal. This is the version, which has not been fully edited and content may change prior to final publication.
Citation information: DOI 10.24425/aee.2026.158257

comprises three key elements: the integration of active rotor impedance into the crowbar circuit, the establishment of dynamic models for both stator and rotor, and the design of a specialised crowbar resistance unit [24]. Xiao *et al.* propose a method that incorporates the DFIG's short-circuit characteristics throughout the entire LVRT process to achieve improved LVRT capability [25]. Qu *et al*. proposed a methodology based on statistical sampling to evaluate the synergistic effects of crowbar resistance values and switching schemes on key parameters, including rotor peak current, DC-link voltage, and reactive power, for the purpose of optimising LVRT strategies [26]. However, when the crowbar protection circuit activates during a fault, it absorbs a significant amount of reactive power from the grid, which is detrimental to the post-fault recovery of grid voltage. Therefore, a significant area of research focuses on integrating diverse compensation devices into the DC-link. The primary goal is to bolster the system's stability and maintain voltage levels during fault conditions [27–29].

As a prominent compensation device, the static synchronous compensator (STATCOM) is extensively used in DFIG's LVRT strategies due to its ability to swiftly regulate reactive power—by controlling its output voltage magnitude and phase—thus ensuring enhanced voltage stability and power quality [30–32].

Energy storage systems (ESSs) can effectively smooth power fluctuations, provide backup power and voltage support, and enhance grid stability and reliability [33]. Batteries exhibit a superior balance of high energy density and comparatively low cost, and suitability for long-duration energy storage; supercapacitors (SCs) feature extremely high-power density and rapid response speed; superconducting magnetic energy storage (SMES) offers fast response, making it suitable for transient compensation and rapid dynamic response [34–36]. Integrating SMES at the DC-link has been shown to enhance the LVRT capability of DFIGs, providing fast-acting support during grid disturbances and improving overall system stability [37, 38]. The study by Xu *et al*. explores a hybrid energy storage strategy, combining supercapacitors with batteries at the DC-link of a DFIG wind farm, to improve transient stability and enhance LVRT resilience [39].

However, despite these advances, recent LVRT-oriented studies still exhibit several limitations. Control-based approaches often depend on accurate system parameters and may lose robustness during severe voltage disturbances. Hardware-oriented schemes such as modified crowbars or fault current limiters can suppress rotor overcurrent but typically absorb substantial reactive power and provide limited support to DC-link energy regulation. Moreover, single-type energy storage configurations cannot simultaneously fulfil the requirements for fast dynamic response and adequate energy buffering under deep voltage sags. These constraints highlight the need for a coordinated strategy that integrates improved protection circuitry with hybrid energy storage.

To address these issues, this paper proposes a coordinated protection scheme that combines a RC-Crowbar circuit with a HESS consisting of batteries and supercapacitors (Fig. 1). The RC-Crowbar is designed to limit rotor overcurrent and DC-link overvoltage during grid faults, while the HESS employs a coordinated control strategy in which supercapacitors provide rapid transient power support and batteries supply sustained energy compensation. Finally,

This paper has been accepted for publication in the AEE journal. This is the version, which has not been fully edited and content may change prior to final publication.
Citation information: DOI 10.24425/aee.2026.158257

MATLAB/Simulink simulation results verify that the proposed scheme significantly enhances the LVRT capability and transient stability of DFIGs under severe fault conditions, offering an effective reference for the secure and reliable operation of large-scale wind farms.

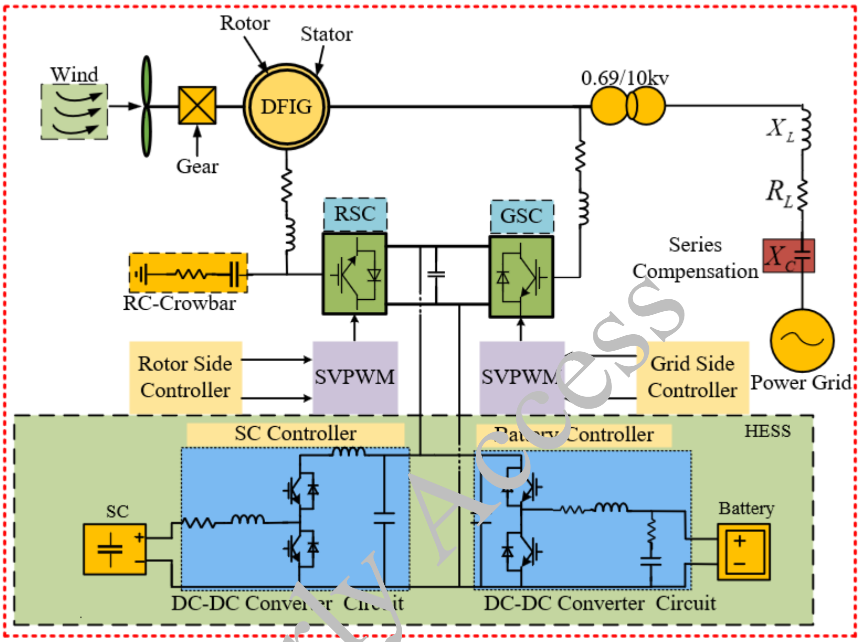

Fig. 1. Topology of the proposed DFIG system integrated with HESS

2. DFIG's transient response to grid faults

Adopting the motor convention and neglecting magnetic saturation, the voltage–flux dynamics of the DFIG in the *d-q* synchronous reference frame can be expressed in vector form as follows [3, 5]:

$$\begin{cases} \boldsymbol{u}_s = R_s \boldsymbol{i}_s + \frac{\mathrm{d}}{\mathrm{dt}} \boldsymbol{\psi}_s + j\omega_s \boldsymbol{\psi}_s \\ \boldsymbol{u}_r = R_r \boldsymbol{i}_r + \frac{\mathrm{d}}{\mathrm{dt}} \boldsymbol{\psi}_r + j(\omega_s - \omega_r)\boldsymbol{\psi}_r, \\ \boldsymbol{\psi}_s = L_s \boldsymbol{i}_s + L_m \boldsymbol{i}_r \\ \boldsymbol{\psi}_r = L_r \boldsymbol{i}_r + L_m \boldsymbol{i}_s \end{cases} \tag{1}$$

where: $\boldsymbol{u}_s = u_{sd} + ju_{sq}$ and $\boldsymbol{u}_r = u_{rd} + ju_{rq}$ are the stator and rotor voltage space vectors; $\boldsymbol{i}_s = \boldsymbol{i}_{sd} + ji_{sq}$ and $\boldsymbol{i}_r = i_{rd} + ji_{rq}$ denote the stator and rotor current space vectors; $\boldsymbol{\psi}_s = \psi_{sd} + j\psi_{sq}$ and $\boldsymbol{\psi}_r = \psi_{rd} + j\psi_{rq}$ represent the stator and rotor flux linkage space vectors. R_s and R_r are the stator and rotor resistances, respectively. ω_s is the synchronous reference-frame angular speed, and ω_r is the rotor electrical angular speed. L_s and L_r are the stator and rotor leakage inductances, and L_m is the mutual inductance between the stator and rotor. The bold symbols in (1) denote space vectors in the synchronous *d-q* reference frame, and the operator *j* represents the associated orthogonal rotation.

The previously established theoretical model yields the equivalent circuit representation for the DFIG during normal operation in the d-q reference frame, which is depicted in Fig. 2.

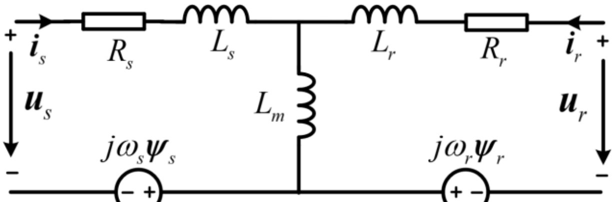

Fig. 2. Equivalent circuit of DFIG

For analytical convenience, the stator flux dynamics during grid voltage sags are expressed in the complex space-vector form, which is mathematically equivalent to the synchronous *d-q* reference frame. In the short-term transient analysis of voltage sags, the stator winding resistance *R_s* is neglected in the proposed dynamic model due to its relatively small magnitude compared with the synchronous reactance. This assumption is consistently applied in the derivation of (2)−(4).

$$\frac{\mathrm{d}\boldsymbol{\psi}_s}{\mathrm{d}t} = \boldsymbol{u}_s - j\omega_s\boldsymbol{\psi}_s. \tag{2}$$

Correspondingly, the rotor-side open-circuit voltage under grid fault conditions can be expressed as:

$$\boldsymbol{u}_{ro} = \frac{\mathrm{d}\boldsymbol{\psi}_r}{\mathrm{d}t} + j(\omega_s - \omega_r)\boldsymbol{\psi}_r. \tag{3}$$

Deriving the DFIG's rotor current during a fault requires solving the space-vector equations in the synchronous d–q reference frame given by (1), (2), and (3) simultaneously.

$$\boldsymbol{i}_r = \frac{1}{R_r + j(\omega_s - \omega_r)\left(L_r - \frac{L_m^2}{L_s}\right)}\left[\boldsymbol{u}_r - \frac{L_m}{L_s}(\boldsymbol{u}_s - j\omega_s\boldsymbol{\psi}_s)\right]. \tag{4}$$

It should be noted that the complex quantities in (2), (3), (4) represent space vectors and are fully consistent with the vector model expressed in the synchronous d–q reference frame in (1).

3. LVRT scheme based on coordinated protection of RC-Crowbar circuit and HESS

This paper has been accepted for publication in the AEE journal. This is the version, which has not been fully edited and content may change prior to final publication.
Citation information: DOI 10.24425/aee.2026.158257

3.1. RC-Crowbar circuit structure

Severe grid faults can cause rotor-side overcurrent in DFIGs [42]. While the conventional crowbar circuit alleviates this issue, it also leads to excessive reactive power absorption due to the DFIG's underdamped transients, hindering post-fault voltage recovery. To address this, an RC-Crowbar is proposed, integrating a series resistor and capacitor. The capacitor supplies reactive power, thereby reducing the DFIG's grid demand and suppressing DC-link voltage surges, which together enhance LVRT performance. The configuration is shown in Fig. 3.

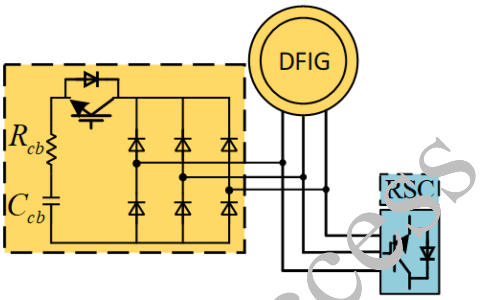

Fig. 3. RC-Crowbar circuit structure

3.2. Rotor current in the RC-Crowbar circuit

Following the theoretical derivations of (1) and (2) presented above, the DFIG's equivalent circuit post-crowbar activation is depicted in Fig. 4.

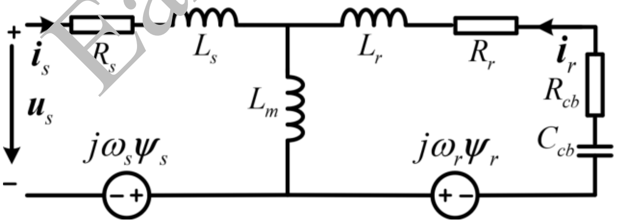

Fig. 4. Equivalent circuit of DFIG after RC-Crowbar activation

Therefore, starting from the space-vector equations in the synchronous *d*-*q* reference frame and in conjunction with the equivalent circuit shown in Fig. 4, assuming a symmetrical grid voltage sag with depth *h* occurring at *t*, the coupled vector equations can be reduced to a scalar analytical form. Accordingly, the transient rotor current [40–42] response after RC-Crowbar activation is given as follows:

$$i_r = \frac{L_m}{L_s}\frac{(1-s)hU_s}{(R_r+R_{cb})-js\omega_r\sigma L_r+\frac{1}{j\omega_r C_{cb}}}\exp\left[-js\omega_r t-\left(\frac{t}{\tau'}\right)\right]+K\exp\left(-\frac{t}{\tau_r'}\right)$$
$$-\frac{L_m}{L_s}\frac{(1-h)sU_s}{(R_r+R_{cb})+js\omega_s\sigma L_r+1/js\omega_s C_{cb}}\exp(js\omega_1 t), \tag{5}$$

where τ and τ_r are the transient time constants of the rotor current determined by the rotor and RC-Crowbar circuit parameters. K is an integration constant determined by the rotor current initial condition at the fault instant. $\sigma = 1 - L_m^2/L_s L_r$ is the leakage coefficient, R_{cb} and C_{cb} are the resistance and capacitance of the RC-Crowbar circuit, respectively. s is the slip of the machine. U_s is the stator voltage magnitude.

Equation (5) provides the selection principles for the values of resistor R_{cb} and capacitor C_{cb} in the RC-Crowbar circuit.

$$C_{cb} = \frac{2 I_{LR}^2 \omega_s}{\omega_r^2 \sqrt{3 U_{rM}^2 I_{LR}^2 - P_{rM}^2}}, \tag{6}$$

$$\begin{cases} U_{r\_\max} = I_{r\_\max} R_{cb} \\ R_{cb} \le \dfrac{U_{dc\_\mathrm{lim}}}{I_{r\_\max}} \end{cases}, \tag{7}$$

where: $I_{r\_\max}$ is the maximum rotor current, $U_{r\_\max}$ is the maximum rotor voltage, U_{dc_lim} is the DC-link bus voltage limit, and I_{LR} is the blocked rotor current. Furthermore, U_{rM} represents the rated rotor voltage, and P_{rM} denotes the rated rotor power.

3.3. LVRT scheme for the DFIG system

Figure 5 illustrates the LVRT control strategy. When the grid voltage falls below 0.9 p.u., the system enters the fault-response mode, in which the GSC and the battery switch to State 1 to provide DC-link support and reactive power compensation. During this process, the RC-Crowbar circuit is triggered if the rotor current exceeds 1.5 p.u. or the DC-link voltage rises above 1.2 p.u., and it is deactivated once the rotor current decreases below 1.4 p.u. or the DC-link voltage drops below 1.1 p.u. After the fault is cleared or the grid returns to normal operation, the GSC and the battery shift to State 2, which is dedicated to managing the DFIG output power.

This paper has been accepted for publication in the AEE journal. This is the version, which has not been fully edited and content may change prior to final publication.
Citation information: DOI 10.24425/aee.2026.158257

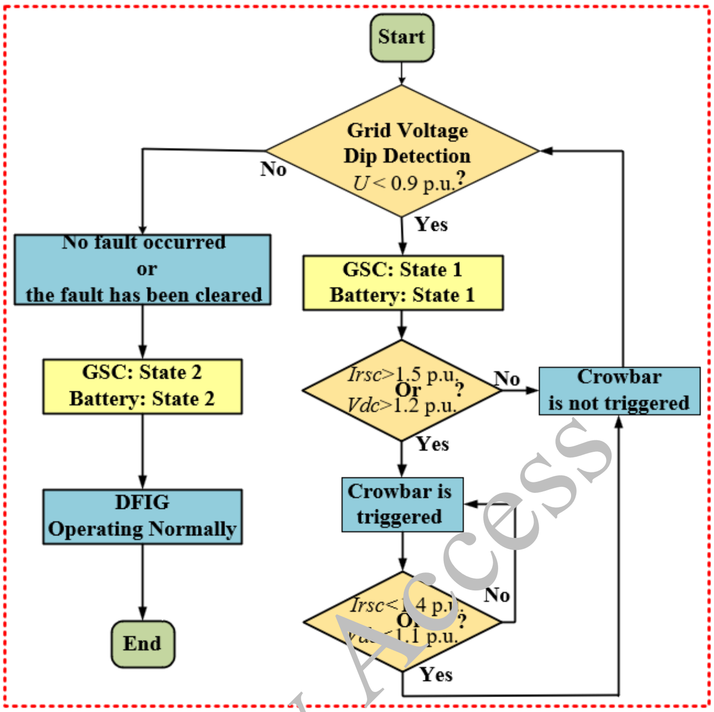

Fig. 5. Flowchart of the LVRT scheme for the DFIG

4. DFIG system control structure

4.1. Control structure of GSC

The GSC in a DFIG system serves two primary functions [9]: it ensures DC-link voltage stability while simultaneously controlling the flow of power to and from the grid. A diagram of this configuration is provided in Fig. 6(a). The GSC control scheme utilised in this paper is outlined subsequently [34]. The operational state of the GSC is divided into State 1 and State 2.

State 1: The onset of a grid fault triggers the activation of the HESS. Afterwards, the HESS delivers voltage support and power compensation to the DFIG throughout the disturbance. Under grid fault conditions, the reference signals for the axis currents are generated from distinct error measurements. Specifically, the d-axis current reference is derived from the DC-link voltage fluctuation, whereas the q-axis current reference is determined by the voltage variation at the point of common coupling (PCC).

State 2: There are no faults, or after a fault is cleared, then the HESS is used to achieve stable operation in the system, and balance active power and reactive power and provides for a certain amount of voltage support. The d- and q-axis current references are determined under normal grid conditions by the measured discrepancies in turbine generation power and reactive power.

This paper has been accepted for publication in the AEE journal. This is the version, which has not been fully edited and content may change prior to final publication.
Citation information: DOI 10.24425/aee.2026.158257

4.2. Control structure of RSC

The RSC of DFIG uses the stator flux-oriented vector control structure, as shown in Fig. 6(b). According to this structure, the active power reference is determined by maximum power point tracking (MPPT) for wind power. The stator's active and reactive powers are independently controlled by the *d*-axis and *q*-axis components of the rotor current, respectively. The rotor voltage command is generated based on the deviation between the reference current and the measured current, and is processed by a PI controller to ensure precise current tracking. This structure not only achieves decoupled control of active and reactive power but also maintains stable system performance across varying wind speeds.

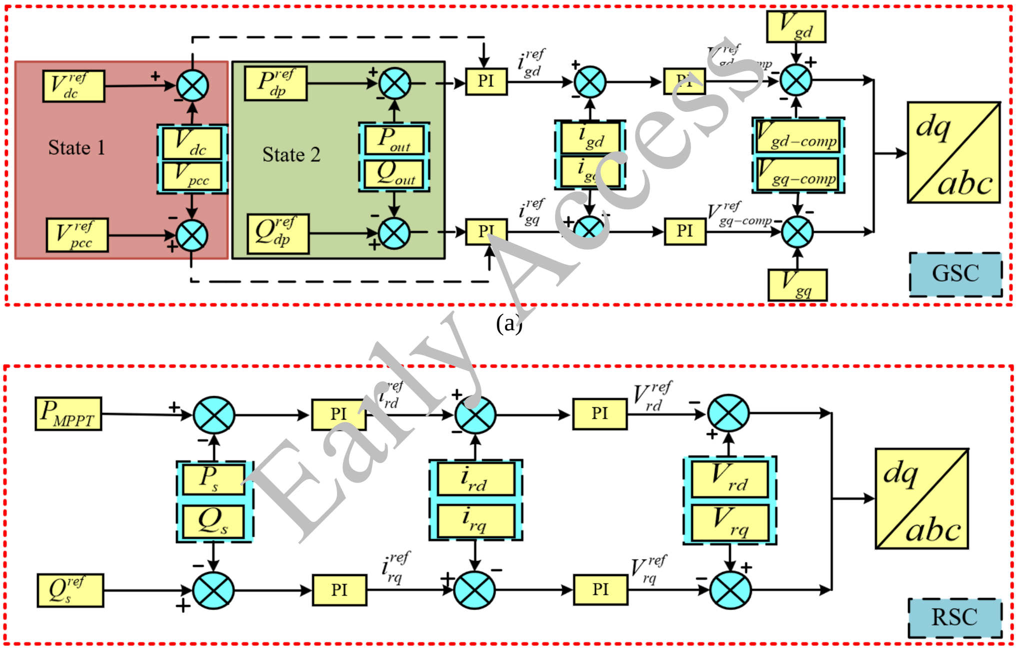

(a)

(b)

Fig. 6. Control structure of the DFIG: control structure of the GSC (a); control structure of the RSC (b)

4.3. Control structure of HESS

In this work, a HESS, comprising both batteries and supercapacitors, is integrated at the DC-link to maintain its voltage stability during fault scenarios. Hence, it is crucial to devise a control structure that effectively governs the power exchange of the batteries and supercapacitors. Such a structure is fundamental to augmenting the overall LVRT performance of the DFIG.

The SC is controlled to stabilise the DC-link voltage by dynamically adjusting its charge and discharge power. The DC-link voltage error is processed through a PI regulator to generate the current reference, which is further constrained by the state of charge (SoC) and voltage limits.

Based on these conditions, the SC operates in either charging mode (in) or discharging mode (out). This structure enables the SC to provide fast energy buffering and effectively suppress DC-link voltage fluctuations.

As illustrated in Fig. 7(b), the battery adopts a dual-mode control structure to provide both DC-link voltage support and power balancing.

In State 1, when a grid fault occurs or the DC-link voltage deviates from its reference, the actual voltage is compared with the reference. The error is processed by a PI regulator to generate the battery power command, enabling the battery to charge or discharge so as to stabilise the DC-link voltage.

In State 2, under normal grid operation, the battery operates in the power-balancing mode. The preliminary reference power is obtained from the deviation between the wind turbine output and the dispatching command. This deviation is then processed by the low-pass filter (LPF) block to generate the final power reference, preventing overload conditions. The obtained reference is converted into current commands, which are tracked through PI controllers equipped with limiters and logical operators. Based on the DC-link voltage conditions, the control system determines whether the battery operates in charging (in) or discharging (out) mode.

This structure allows the battery to provide fast DC-link voltage support during disturbances and to ensure active power management during normal operation, while avoiding overcharge or deep discharge.

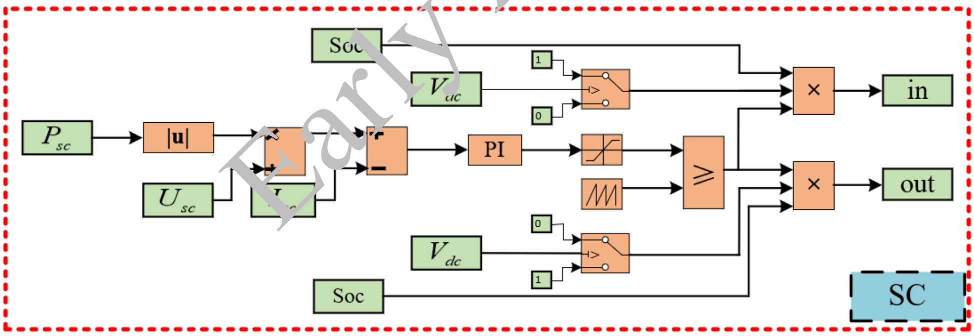

(a)

This paper has been accepted for publication in the AEE journal. This is the version, which has not been fully edited and content may change prior to final publication.
Citation information: DOI 10.24425/aee.2026.158257

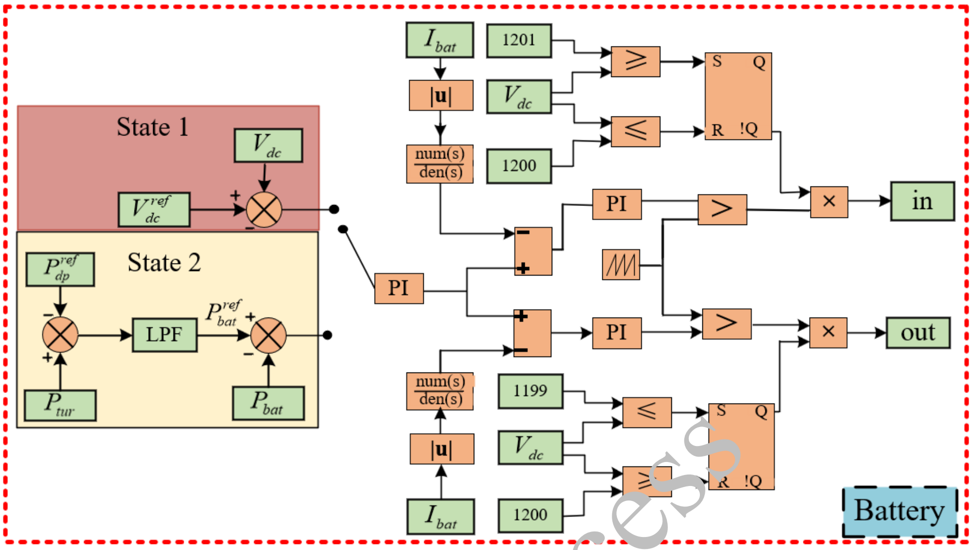

(b)

Fig. 7. Control structure of the HESS: control structure for the SC (a); control structure for the battery (b)

5. Simulation results and discussion

A comprehensive simulation testbed, established in MATLAB/Simulink, was employed to assess the effectiveness of the proposed strategy. The model consists of several key components: the RSC, GSC, the DFIG itself, a crowbar protection circuit, and an energy storage system. In the simulation model, the battery and supercapacitor are interfaced with the DC-link through DC/DC converters, enabling power exchange between the low-voltage energy storage units and the 1 200 V DC-link. Simulations were performed to validate the proposed scheme's effectiveness in enhancing the DFIG's LVRT performance during grid faults.

The detail parameters of the DFIG: rated power P_n = 2 000 kW, rated voltage U_n = 690 V, rated speed n = 1 500 r/min, L_s = 12.5 mH, L_r = 11.8 mH, L_m = 10.5 mH, R_s = 0.012 Ω, R_r = 0.01 Ω, DC-link voltage V_{dc} = 1 200 V. The PI parameters of the converters are as follows: for the RSC, the outer-loop PI controllers use $K_p = 2$, $K_i = 10$, and the inner current-loop PI controllers use $K_p = 15$, $K_i = 20$; for the GSC, the outer-loop PI gains are $K_p = 2$, $K_i = 100$, and the inner-loop PI gains are $K_p = 15$, $K_i = 200$.

The HESS consists of a lithium-ion battery (24 V, 14 Ah, 60% initial SoC, 0.08 s response time) and an electric double-layer supercapacitor (32 V, 29 F, 31.5 V initial voltage, 0.001 s response time). Both the battery and the supercapacitor are connected to the DC-link through bidirectional DC/DC converters, which enable voltage matching and controlled power exchange between the low-voltage energy storage units and the high-voltage DC-link. As a result, the power shown in the simulations corresponds to the regulated equivalent DC-link-side response, rather than direct instantaneous power delivery from the low-voltage sources. The SoC is modelled using a conventional coulomb-counting method, given by:

$$\mathrm{SOC}(t) = \mathrm{SOC}(t_0) - \frac{1}{C_{\mathrm{bat}}}\int_{t_0}^{t} I_{\mathrm{bat}}(\tau)\,\mathrm{d}\tau, \tag{8}$$

where C_{bat} denotes the battery capacity and I_{bat} is the battery current. In the simulations, the battery SoC is constrained within predefined limits, and the battery power reference is limited when the SoC approaches its upper or lower bound.

The PI parameters of the HESS controllers are configured as follows. The supercapacitor employs a PI regulator with $K_p = 1$, $K_i = 0.01$. The battery control includes one outer loop, with $K_p = 2$, $K_i = 1.5$, and two inner loops, whose parameters, from top to bottom in the control diagram, are $K_p = 0.1$, $K_i = 0.1$ and $K_p = 0.2$, $K_i = 0.1$, respectively.

The simulation fault is set as a symmetrical three-phase short-circuit to ground fault, with the fault-induced voltage drop at 80%, 60%, 40%. This period was divided into three distinct time segments: t_0, t_1, t_2.

t_0 [0.3 s $\leq t < 1$ s]: The DFIG simulation model operates under normal conditions.

t_1 (1 s $\leq t \leq 1.625$ s]: A three-phase short-circuit to ground fault occurs, and the grid voltage drops.

t_2 (1.625 s $< t < 2.5$ s]: The fault is cleared and the grid returns to normal.

5.1. Verification of the effectiveness

Figure 8 compares the performance of the traditional resistive crowbar and the proposed RC-Crowbar circuit, evaluating key variables such as stator voltage, stator current, rotor current under a severe fault condition characterized by an 80% voltage drop.

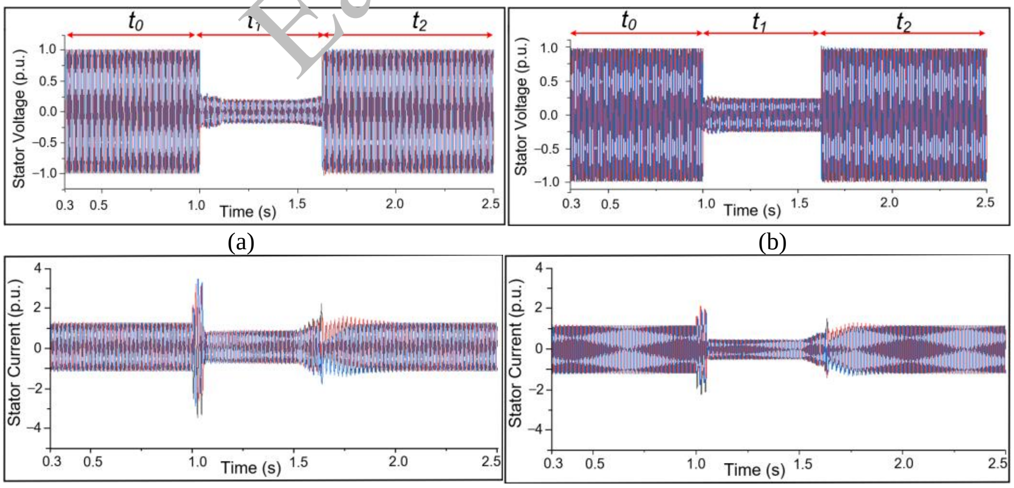

(a) (b)

(c) (d)

This paper has been accepted for publication in the AEE journal. This is the version, which has not been fully edited and content may change prior to final publication.
Citation information: DOI 10.24425/aee.2026.158257

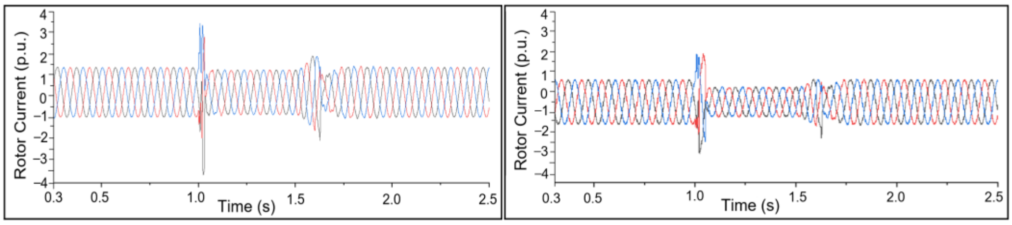

(e) (f)

Fig. 8. Performance comparison under an 80% voltage drops: stator voltage (R-Crowbar) (a); stator voltage (RC-Crowbar) (b); stator current (R-Crowbar) (c); stator current (RC-Crowbar) (d); rotor current (R-Crowbar) (e); rotor current (RC-Crowbar) (f)

As depicted in Fig. 8, both crowbar circuits ensure the DFIG's compliance with LVRT requirements. However, the conventional resistive variant impedes post-fault system restoration by consuming reactive power from the grid. This difference is evident in several key metrics. Upon fault clearance at 1.625 s, the stator voltage with the traditional crowbar recovers only to approximately 0.9 p.u. and reaches its nominal value around 1.8 s [Fig. 8(a)]. In contrast, the RC-Crowbar enables faster voltage recovery and maintains a smoother waveform throughout the fault [Fig. 8(b)]. Moreover, the proposed circuit reduces stator current oscillations during the fault and mitigates rotor current transients after the fault, which can help accelerate the return to stable operation [Fig. 8(c–f)].

Figure 9 presents a comparison of the power responses and DC-link voltage performance under an 80% grid voltage sag for three schemes: the traditional crowbar, the RC-Crowbar, and the RC-Crowbar combined with HESS. The Fig. 9 also illustrates the effective triggering of the crowbar circuit under this fault condition.

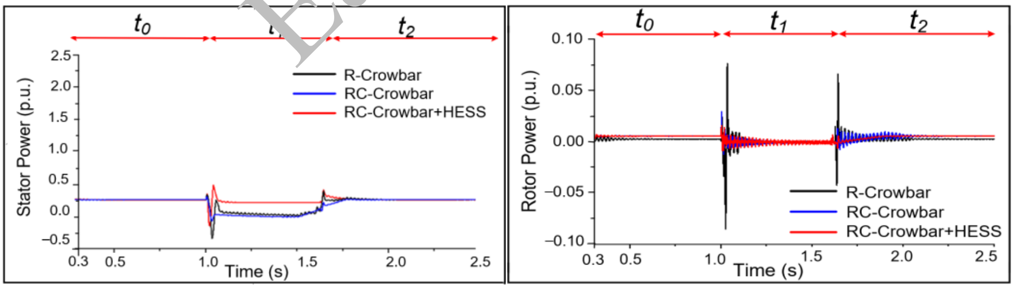

(a) (b)

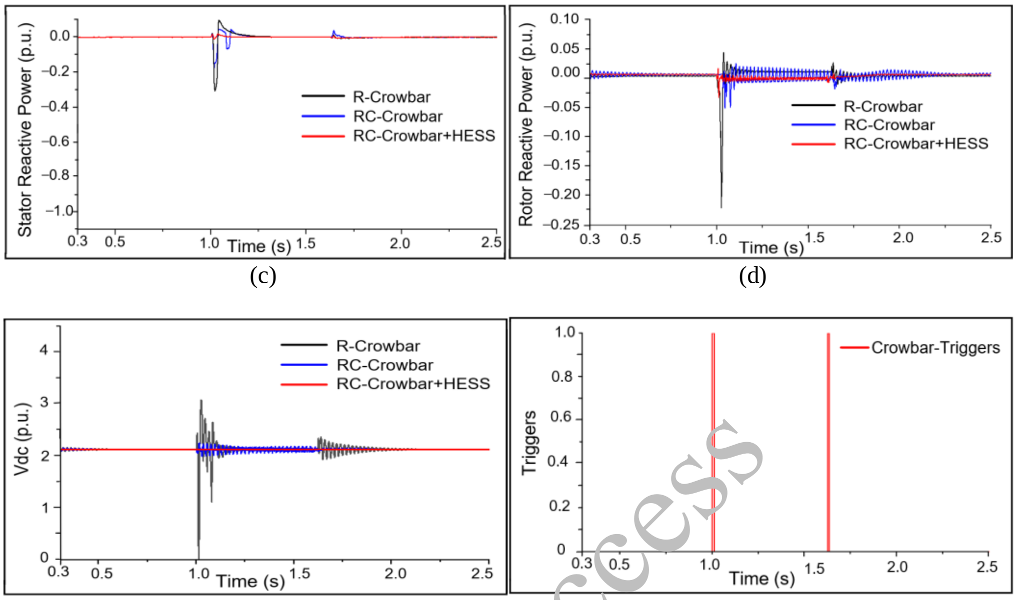

(c) (d)

(e) (f)

Fig. 9. Comparison of power response and DC-link voltage performance under an 80% grid voltage sag: traditional crowbar, RC-Crowbar, and RC-Crowbar with the HESS scheme; along with the effective triggering of the crowbar circuit: stator power (a); rotor power (b); stator reactive power (c); rotor reactive power (d); DC-link voltage (e); crowbar-triggers (f)

As shown in Fig. 9(a–e), the power responses and DC-link voltage performance under different protection schemes exhibit notable differences. For the stator active power [Fig. 9(a)], the RC-Crowbar and R-Crowbar provide comparable protection, while the RC-Crowbar combined with HESS mitigates the power drop by approximately 0.2 p.u. Regarding rotor active power [Fig. 9(b)], the RC-Crowbar reduces the oscillation amplitude by about 0.04 p.u. relative to the R-Crowbar, whereas the RC-Crowbar with HESS scheme achieves a larger reduction of nearly 0.06 p.u. and shortens the recovery time by around 0.35 s. For the stator reactive power [Fig. 9(c)], the RC-Crowbar reduces the initial oscillation amplitude by approximately 0.2 p.u. compared with the R-Crowbar, whereas the RC-Crowbar with HESS scheme achieves a larger reduction of about 0.4 p.u. in the early stage of the fault and shortens the recovery time by roughly 0.1 s. For rotor reactive power [Fig. 9(d)], the RC-Crowbar decreases the oscillation amplitude by roughly 0.17 p.u., and the RC-Crowbar with HESS scheme further reduces it by about 0.19 p.u., with the recovery time shortened by approximately 0.5 s. In terms of the DC-link voltage [Fig. 9(e)], the RC-Crowbar suppresses the oscillation by about 1.8 p.u. compared with the R-Crowbar, while the RC-Crowbar with HESS reduces it by nearly 2 p.u., resulting in almost no fluctuation during the fault and a recovery time shortened by about 0.4 s.

Figure 9(f) further verifies the effective triggering of the crowbar circuit. At the onset of the fault, the crowbar is promptly activated to limit rotor overcurrent, and after fault clearance, it is

This paper has been accepted for publication in the AEE journal. This is the version, which has not been fully edited and content may change prior to final publication.
Citation information: DOI 10.24425/aee.2026.158257

effectively re-triggered when the rotor current surges again, thereby ensuring continuous system protection.

To further validate the effectiveness of the proposed method, Fig. 10 presents a comparison of the power responses under a 60% grid voltage drop. The results indicate that the proposed method can effectively improve power stability compared with the traditional crowbar.

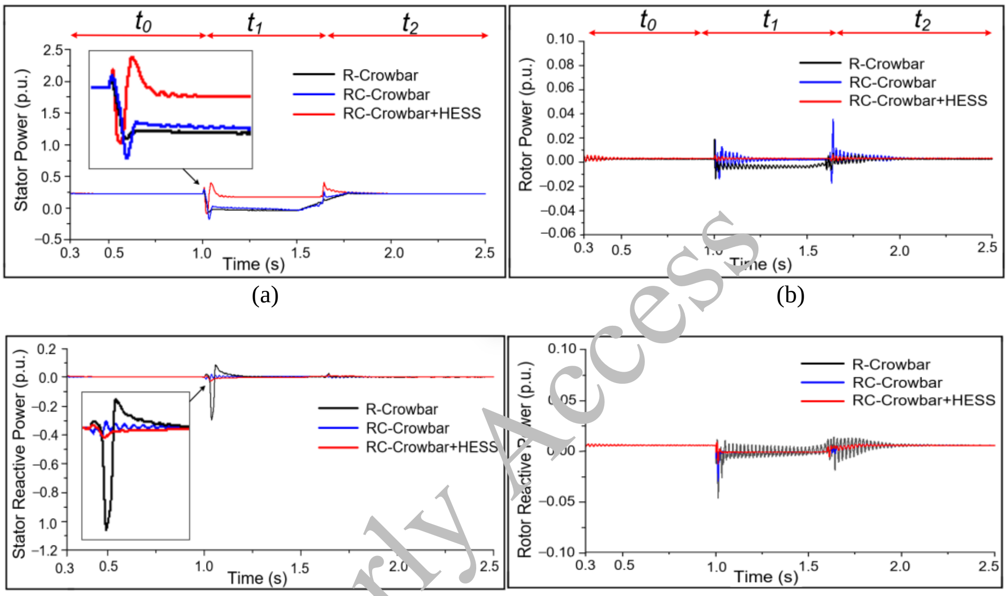

(a) (b)

(c) (d)

Fig. 10. Comparison of stator and rotor power responses under a 60% grid voltage drop: traditional crowbar, RC-Crowbar, and RC-Crowbar with the HESS scheme: stator power (a); rotor power (b); stator reactive power (c); rotor reactive power (d)

As shown in Fig. 10(a–d), the RC-Crowbar reduces the initial oscillation of the stator active power by approximately 0.05 p.u. compared with the R-Crowbar, while the RC-Crowbar combined with HESS mitigates the power drop by about 0.2 p.u. throughout the entire fault. For the rotor active power, the RC-Crowbar decreases the oscillation amplitude by nearly 0.01 p.u., whereas the RC-Crowbar with HESS scheme further reduces it by around 0.015 p.u. and shortens the recovery time by approximately 0.35 s. Regarding the stator reactive power, the RC-Crowbar lowers the initial oscillation by roughly 0.2 p.u., while the (RC-Crowbar with HESS) scheme achieves almost fluctuation-free performance during the fault. In terms of rotor reactive power, the RC-Crowbar suppresses the oscillation amplitude by about 0.02 p.u., and the RC-Crowbar with HESS scheme further decreases it by nearly 0.04 p.u., with the recovery time shortened by approximately 0.2 s.

Figure 11 presents the stator and rotor power responses under a 40% grid voltage drop, further demonstrating the effectiveness of the proposed method under this voltage sag condition.

This paper has been accepted for publication in the AEE journal. This is the version, which has not been fully edited and content may change prior to final publication.
Citation information: DOI 10.24425/aee.2026.158257

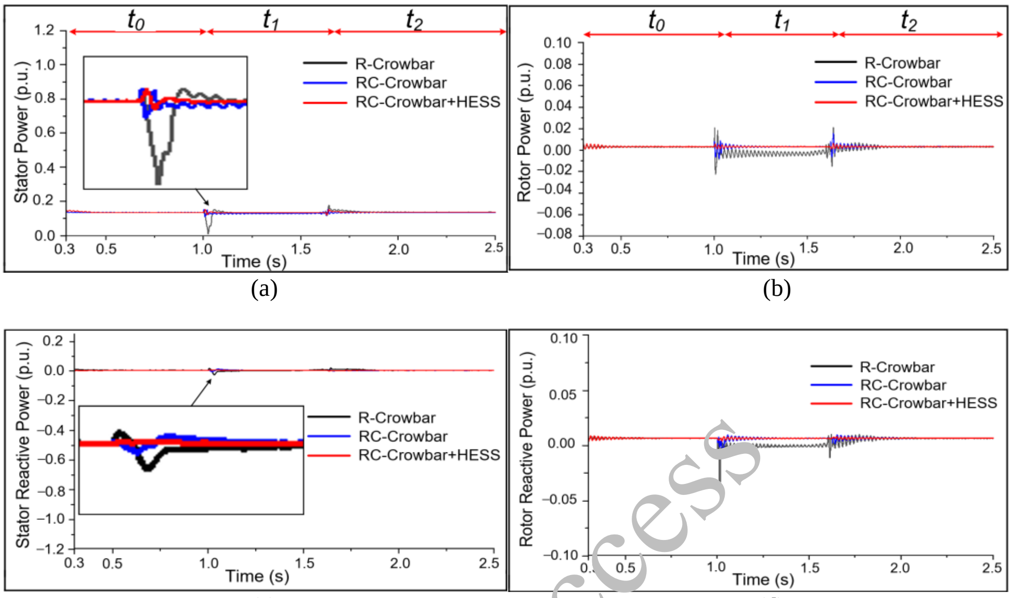

(a) (b)

(c) (d)

Fig. 11. Comparison of stator and rotor power responses under a 40% grid voltage drop: traditional crowbar, RC-Crowbar, and RC-Crowbar with the HESS scheme: stator power (a); rotor power (b); stator reactive power (c); rotor reactive power (d)

As shown in Fig. 11(a–d), the RC-Crowbar suppresses the initial oscillation of the stator active power by approximately 0.15 p.u. compared with the R-Crowbar, while the RC-Crowbar combined with HESS maintains nearly fluctuation-free performance throughout the entire fault, with the recovery time shortened by about 0.2 s. For the rotor active power [Fig. 11(b)], the RC-Crowbar decreases the oscillation amplitude by nearly 0.01 p.u., whereas the RC-Crowbar with HESS scheme eliminates the oscillation during the fault and further reduces the recovery time by approximately 0.3 s. Regarding the stator reactive power [Fig. 11(c)], the RC-Crowbar lowers the initial oscillation by about 0.02 p.u. before stabilising with almost no fluctuation, while the RC-Crowbar with HESS scheme achieves nearly fluctuation-free performance for the entire fault duration. In terms of rotor reactive power [Fig. 11(d)], the RC-Crowbar reduces the initial oscillation by roughly 0.02 p.u. compared with the R-Crowbar, whereas the RC-Crowbar with HESS scheme decreases it by about 0.04 p.u., limits the overall fluctuation by around 0.01 p.u. and shortens the recovery time by approximately 0.2 s.

Figure 12 shows the power output of the battery and supercapacitor under different grid voltage dips (80%, 60%, 40%).

This paper has been accepted for publication in the AEE journal. This is the version, which has not been fully edited and content may change prior to final publication.
Citation information: DOI 10.24425/aee.2026.158257

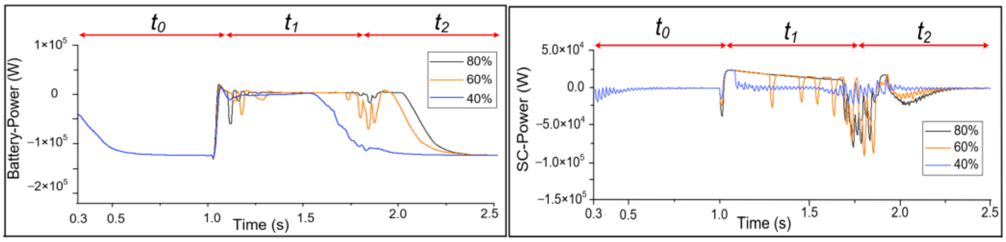

(a) (b)

Fig. 12. Power outputs of the battery and supercapacitor under different grid voltage sags: power outputs of the battery (a); power outputs of the supercapacitor (b). The shown power corresponds to the equivalent DC-link-side power through DC/DC interfacing

As shown in Fig. 12, when the grid voltage drops to 80%, the battery provides the maximum power support, with a larger power fluctuation that lasts for a longer time. As the voltage drop decreases, the power fluctuation of the battery decreases, and the recovery time also shortens accordingly. It should be noted that the reported power values correspond to short-duration equivalent DC-link-side power through DC/DC interfacing and do not directly reflect the rated power of the energy storage units.

In contrast, the supercapacitor responds more quickly, especially in the initial phase of the voltage drop, where it mainly provides instantaneous power support. With an 80% voltage drop, the power fluctuation of the Supercapacitor is larger, but its recovery speed is faster. At a 40% voltage drop, the power fluctuation is the smallest, and the recovery is rapid.

This indicates that the battery and Supercapacitor play different roles in the HESS system: the battery mainly provides long-term power support, while the supercapacitor handles short-term instantaneous power demands. Together, they effectively stabilise the power output on the DC-link side.

5.2. Discussion

The experimental results indicate that the proposed RC-Crowbar coordinated with the HESS provides significant advantages in the LVRT of DFIG wind turbines. Compared with the traditional crowbar and RC-Crowbar schemes, it effectively suppresses oscillations in stator and rotor power and stabilises the DC-link voltage, enabling faster system recovery during faults.

In terms of effectiveness, the RC-Crowbar enhances energy absorption through its resistor–capacitor design, avoiding the large power oscillations and slow recovery seen in traditional schemes. The addition of HESS provides an extra energy regulation pathway, allowing smoother power output and improving the wind turbine's ride-through capability.

Regarding accuracy, the model reasonably captures the dynamic behaviour of the DFIG under different voltage sag conditions. Trends in active and reactive power, as well as DC-link voltage responses, are consistent with the expected physical mechanisms, indicating reliable representation of key dynamics.

Overall, the RC-Crowbar with HESS scheme demonstrates clear improvements in efficiency, effectiveness, and accuracy, offering a practical solution to enhance fault ride-through capability.

This paper has been accepted for publication in the AEE journal. This is the version, which has not been fully edited and content may change prior to final publication.
Citation information: DOI 10.24425/aee.2026.158257

Future work should consider wind farm cluster operation, complex grid conditions, and energy storage capacity optimisation to further validate the approach.

6. Conclusion

This paper proposes a coordinated LVRT protection strategy for DFIGs based on an enhanced RC-Crowbar circuit and a HESS. Compared with the traditional resistive crowbar, the improved RC-Crowbar utilizes its capacitive branch to provide reactive power support, effectively suppressing rotor overcurrent and DC-link overvoltage while reducing reactive power absorption during grid faults. The HESS, consisting of batteries and supercapacitors, provides long-term energy compensation and fast dynamic support, thereby maintaining DC-link voltage stability and smoothing power fluctuations.

At an 80% voltage sag, the RC-Crowbar circuit reduces the rotor current oscillation amplitude by approximately 0.4 p.u. during the fault and shortens the recovery time by about 0.3 s. When coordinated with the HESS, the DC-link voltage fluctuation is further suppressed by around 2 p.u., the voltage recovery speed increases by 20%–25%, and the reactive power oscillation amplitude decreases by about 0.4 p.u., indicating a significant improvement in transient stability and dynamic performance.

Compared with existing LVRT strategies, the proposed coordinated protection scheme achieves comprehensive improvements in fault current suppression, voltage stability, and recovery speed, overcoming the limitations of single-type protection measures and exhibiting excellent dynamic and steady-state performance. Overall, the coordinated control of the RC-Crowbar and HESS provides a feasible and engineering-oriented solution for enhancing the LVRT capability of DFIGs and ensuring stable grid operation. Future work will focus on optimising energy storage capacity allocation, developing coordinated control for multi-turbine systems, and exploring adaptive control strategies under complex grid conditions to further improve the overall performance of wind farms.

Acknowledgements

The paper was supported by the National Natural Science Foundation of China (Project No. 62541316), Lanzhou Youth Science and Technology Talent Innovation Project (Project No. 2024-QN-199).

References

[1] Kumar R.K., Choudhary J., *Design of a novel control scheme for the operation of the doubly fed induction generator*, Archives of Electrical Engineering, vol. 73, no. 2, pp. 373–392 (2024), DOI: 10.24425/aee.2024.149922.

[2] Yu W., Huang S.D., Jiang D., *A fault monitoring method for wind power generation system based on sliding mode observer*, Archives of Electrical Engineering, vol. 69, no. 3, pp. 625–643 (2020), DOI: 10.24425/aee.2020.133922.

This paper has been accepted for publication in the AEE journal. This is the version, which has not been fully edited and content may change prior to final publication.
Citation information: DOI 10.24425/aee.2026.158257

[3] Moumani Y., Jabal Laafou A., Ait Madi A., *A comparative study based on proportional integral and backstepping controllers for doubly fed induction generator used in wind energy conversion system*, Archives of Electrical Engineering, vol. 72, no. 1, pp. 211–228 (2023), DOI: 10.24425/aee.2023.143698.

[4] Gołębiowski M., *Optimal control of a doubly fed induction generator of a wind turbine in cooperation with weak and rigid grids*, Archives of Electrical Engineering, vol. 73, no. 3, pp. 681−701 (2024), DOI: 10.24425/aee.2024.150890.

[5] Aman M., Konduparty P., Sharma S., Srivastava R.P., Bhattacharyya S., Sharma V., Balani K., Jha S.K., Omar S., *Layered double hydroxide-based composites for energy storage applications: Insights into supercapacitors and batteries*, Journal of Energy Storage, vol. 116, no. 116093 (2025), DOI: 10.1016/j.est.2025.116093.

[6] Zhao H., Zhang S., Yang L., Xu Z., *Low-voltage ride-through technologies of wind turbines with DFIG: Progress, challenges, and future trends*, Applied Energy, vol. 345, no. 121278 (2023), DOI: 10.1016/j.apenergy.2023.121278.

[7] Chen Y., Liu H., Gao F., Wang K., *Review of fault ride-through control strategies for DFIG-based wind turbines in modern power systems*, IET Renewable Power Generation, vol. 15, no. 12, pp. 2503−2518 (2021), DOI: 10.1049/rpg2.13036.

[8] Luo Y., Yao J., Yang D., Xie H., Zhao L., Jin R., *Improved LVRT strategy for DFIG-based wind turbine considering RSC–GSC interaction during symmetrical grid faults*, IEEE Transactions on Energy Conversion, vol. 40, no. 1, pp. 1–10 (2025), DOI: 10.1109/TEC.2025.3538318.

[9] Marri M.I., Malik N.U.R., Masud M., Jumani T.A., Khidrani A.U., Shahid Z., *Reinforcement learning-based current compensation for brushless doubly fed induction generators under transient- and low-voltage ride-through faults*, Energies, vol. 18, no. 4, 881 (2025), DOI: 10.3390/en18040881.

[10] Chakraborty A., Maity T., *A novel application of adaptive filtering algorithm for LVRT capability enhancement of grid-connected DFIG-based wind energy conversion systems (WECS)*, Electric Power Systems Research, vol. 217, no. 109179 (2023), DOI: 10.1016/j.epsr.2023.109179.

[11] Uddin M.N., Arifin M.S., Rezaei N., *A novel neuro-fuzzy based direct power control of a DFIG-based wind farm incorporated with distance protection scheme and LVRT capability*, IEEE Transactions on Industrial Applications, vol. 59, no. 5, pp. 5792–5803 (2023), DOI: 10.1109/TIA.2023.3270156.

[12] Guan L., Yao J., *A novel PLL structure for dynamic stability improvement of DFIG-based wind energy generation systems during asymmetric LVRT*, Journal of Modern Power Systems and Clean Energy, vol. 11, no. 4, pp. 1149–1164 (2023), DOI: 10.35833/MPCE.2023.000101.

[13] Wang T., Zhu Z., Nian H., *Review of operation technology of doubly-fed induction generator-based wind power system under nonideal grid conditions*, Transactions of China Electrotechnical Society, vol. 35, no. 3, pp. 455–471 (2020).

[14] Nie Y., Liu T., Cai G., Gao L., Wu F., Wang Z., *Low-voltage ride-through handling in doubly fed induction generators based on model-predictive rotor current control*, Power System Technology, vol. 46, no. 3, pp. 905–914 (2022).

[15] Gu J., Zhao R., He J., Xu J., Yan Q., Sun C., Liu H., *Enhanced excitation converter with parallel/series DC-link based on TAB for DFIG to improve the LVRT capability under severe grid faults*, IEEE Transactions on Power Electronics, vol. 38, no. 10, pp. 12304–12308 (2023), DOI: 10.1109/TPEL.2023.3174567.

[16] Ghorbani M., Firouzi M., Mozafari B., Golshan F., *Power flow management and LVRT enhancement by using multi-functional capacitive bridge-type fault current limiter in DFIG system*, International Journal of Electrical Power & Energy Systems, vol. 148, no. 108810 (2023), DOI: 10.1016/j.ijepes.2022.108810.

[17] Liang C., Zhu Y., Zhang Y., Yin K., Xia R., Guan Y., Wang S., *Optimization of the string impedance on the stator side of the DFIG*, Power System Protection and Control, vol. 52, no. 11, pp. 137–147 (2024).

This paper has been accepted for publication in the AEE journal. This is the version, which has not been fully edited and content may change prior to final publication.
Citation information: DOI 10.24425/aee.2026.158257

[18] Du K., Ma X., Zheng Z., Li C., Hu W., Dong K., *LVRT capability improvement of DFIG-based wind turbines with a modified bridge-resistive-type SFCL*, IEEE Transactions on Applied Superconductivity, vol. 31, no. 8, 5603005 (2021), DOI: 10.1109/TASC.2021.3091114.

[19] Zheng Z.-X., Huang C.-J., Yang R.-H., Xiao X.-Y., Li C.-S., *A low voltage ride through scheme for DFIG-based wind farm with SFCL and RSC control*, IEEE Transactions on Applied Superconductivity, vol. 29, no. 2, no. 5601005 (2019), DOI: 10.1109/TASC.2019.2891687.

[20] Zhou B., Dong S., Lin N., Liu S., Yuan J., Shi M., *Analysis of double-fed wind turbine's secondary high voltage ride-through characteristics considering the crowbar circuit*, Power System Protection and Control, vol. 47, no. 5, pp. 152–159 (2020), DOI: 10.35023/j.pspc.2020.05.019.

[21] Dayo S.A., Memon A., Memon Z.A., Jumani T.A., *A new approach for improving dynamic fault ride through capability of grid-tied wind turbines*, Scientific Reports, vol. 15, no. 89396 (2025), DOI: 10.1038/s41598-025-89123-0.

[22] Zhang Y., Zhang J., Li C., Ou J., Zhao W., Zhang S., *Voltage sag evaluation in power grids considering the voltage support capabilities of doubly-fed wind farms during LVRT*, IEEE Transactions on Power Delivery, vol. 40, no. 3, pp. 1540–1553 (2025), DOI: 10.1109/TPWRD.2025.3056789.

[23] Xian L., Wu L., Li W., Wu Y., Xie X., *Enhancing FRT capability of DFIG based on RC-crowbar considering the resonance and matching control strategies for different fault degrees*, Electric Power Systems Research, vol. 232, no. 110434 (2024), DOI: 10.1016/j.epsr.2024.110434.

[24] Wang J., Wang D., Zhao J., Hu H., Liu Q., *Low voltage ride through control strategy for doubly fed asynchronous wind turbines based on super-capacitors*, IEEE Transactions on Renewable Power Generation, pp. 1–9 (2023), DOI: 10.1109/TRPG.2023.10324586.

[25] Döşoğlu M.K., *Crowbar hardware design enhancement for fault ride through capability in doubly fed induction generator-based wind turbines*, ISA Transactions, vol. 104, pp. 321–328 (2020), DOI: 10.1016/j.isatra.2019.11.022.

[26] Xiao F., Xia Y., Zhang K., Zhang Z., Yin X., *Fault characteristics analysis of DFIGWT in whole LVRT process considering control strategy switching between RSC and Crowbar*, International Journal of Electrical Power & Energy Systems, vol. 145, no. 108615 (2023), DOI: 10.1016/j.ijepes.2022.108615.

[27] Yanbin Y., Le G., Guangfu M., Huihui S., Shitao W., *Crowbar resistance value - switching scheme conjoint analysis based on statistical sampling for LVRT of DFIG*, Journal of Modern Power Systems and Clean Energy, vol. 7, no. 3, pp. 558–567 (2019), DOI: 10.35833/MPCE.2019.000024.

[28] Zheng Z., Song D., Du K., Xiao X., Xie Q., *A continuous fault ride-through scheme for DFIGs under commutation failures in LCC-HVDC transmission systems*, IEEE Trans. Energy Convers., vol. 37, no. 6 (2022), DOI: 10.1109/TEC.2022.9808349.

[29] Fouad A., Kotb H., Aboras K.M., Elrefaie H.B., Alqarni M., Baqasah A.M., Yakout A.H., *Enhancing grid-connected DFIG's LVRT capability using dandelion optimizer based the hybrid fractional-order PI and PI controlled STATCOM*, IEEE Access, vol. 12, pp. 120181–120197 (2024), DOI: 10.1109/ACCESS.2024.3427008.

[30] Camargo R.S., Amorim A.E.A., Bueno E.J., Encarnação L.F., *Novel multilevel STATCOM for power system stability enhancement on DFIG-based wind farms*, Electric Power Systems Research, vol. 197, no. 107316 (2021), DOI: 10.1016/j.epsr.2021.107316.

[31] Sayahi K., Bouallegue B., Baazouzi M., Bacha F., *STATCOM and DFIG reactive power management strategy for LVRT capability enhancement under asymmetrical grid faults*, International Journal of Energy Research, no. 7613713 (2025), DOI: 10.1002/er.7613713.

[32] Hete R.R., Mishra S.K., Dash R., Jyotheeswara Reddy K., Subburaj V., Dhanamjayulu C., *Design and analysis of DFIG-STATCOM coordinated P2P grid connected system using RMSProp*, Sustainability, vol. 14, no. 22, no. 15105 (2022), DOI: 10.3390/su142215105.

[33] Li C., Cao Y., Li B., Liu B., Qiao F., Chen P., *A novel low voltage ride-through scheme for DFIG based on the cooperation of hybrid energy storage system and crowbar circuit*, Journal of Energy Storage, vol. 73, 108879 (2023), DOI: 10.1016/j.est.2023.108879.

This paper has been accepted for publication in the AEE journal. This is the version, which has not been fully edited and content may change prior to final publication.
Citation information: DOI 10.24425/aee.2026.158257

[34] Nazaralizadeh S., Banerjee P., Srivastava A.K., Famouri P., *Battery energy storage systems: a review of energy management systems and health metrics*, Energies, vol. 17, no. 5, 1250 (2024), DOI: 10.3390/en17051250.

[35] Mukherjee P., Rao V.V., *Superconducting magnetic energy storage for stabilizing grid integrated with wind power generation systems*, Journal of Modern Power Systems and Clean Energy, vol. 7, no. 2, pp. 400–411 (2019), DOI: 10.1007/s40565-018-0460-y.

[36] Jiang H., Zhou T., Jia Y., Chen J., Zhang C., Zhou Z., Xue J., *Adaptive deactivating control strategy of Crowbar for LVRT capability enhancement of DFIG*, Electrical Power Automation Equipment, vol. 38, no. 9, pp. 93–98 (201.

[37] Bhutto J.K., Abro A.G., Shaikh M.S., Tunio M.A., *An adaptive controlled STATCOM and SMES for LVRT augmentation of the renewable integrated AC-microgrid*, Heliyon, vol. 11, no. 2, e27984 (2025), DOI: 10.1016/j.heliyon.2025. e27984.

[38] Xu J., Zhou X., Li C., Sun Y., Wang H., *A novel hybrid energy storage system based on supercapacitor and battery for DFIG wind farm: transient stability analysis and experimental verification*, Applied Energy, vol. 295, 117043 (2021), DOI: 10.1016/j.apenergy.2021.117043.

[39] Shuja A., Khan H.R., Murtaza I., Ashraf S., Abid Y., Farid F., Sajid F., *Supercapacitors for energy storage applications: materials, devices and future directions – a comprehensive review*, Journal of Alloys and Compounds, vol. 1009, no. 176924 (2024), DOI: 10.1016/j.jallcom.2024.176924.

[40] Yang X., Shu H., Shan J., Sun S., Wang C., *Short circuit current analysis of DFIG considering resistance-capacitance type crowbar protection action time*, Transactions of China Electrotechnical Society, vol. 36, no. 22, pp. 4716–4725 (2021).

[41] Feng H., Shu H., Yang X., Song J., Deng H., Zhou Z., Chen Y., Zhang P., *Synergetic control and fault characteristics analysis of hybrid wind farm considering resistance-capacitance crowbar*, Power Systems Protection and Control, vol. 52, no. [illegible], pp. 111–122 (2024).

[42] Jiang H., Fan Z., Chen J., *Low voltage ride through method of DFIG-based wind turbines by dynamically adjusting crowbar resistance of rotor*, Automation of Electric Power Systems, vol. 42, no. 1, pp. 52–62 (2018).